

# Exchange-Mediated Transport in Battery Electrolytes: Ultrafast or Ultraslow?

Bogdan Dereka, Nicholas H. C. Lewis, Yong Zhang, Nathan T. Hahn, Jonathan H. Keim, Scott A. Snyder, Edward J. Maginn, and Andrei Tokmakoff\*



Cite This: *J. Am. Chem. Soc.* 2022, 144, 8591–8604



Read Online

ACCESS |



Metrics & More

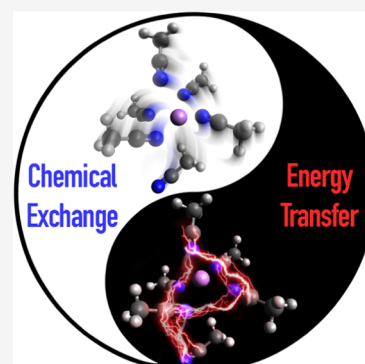


Article Recommendations



Supporting Information

**ABSTRACT:** Understanding the mechanisms of charge transport in batteries is important for the rational design of new electrolyte formulations. Persistent questions about ion transport mechanisms in battery electrolytes are often framed in terms of vehicular diffusion by persistent ion–solvent complexes versus structural diffusion through the breaking and reformation of ion–solvent contacts, i.e., solvent exchange events. Ultrafast two-dimensional (2D) IR spectroscopy can probe exchange processes directly via the evolution of the cross-peaks on picosecond time scales. However, vibrational energy transfer in the absence of solvent exchange gives rise to the same spectral signatures, hiding the desired processes. We employ 2D IR on solvent resonances of a mixture of acetonitrile isotopologues to differentiate chemical exchange and energy-transfer dynamics in a comprehensive series of  $\text{Li}^+$ ,  $\text{Mg}^{2+}$ ,  $\text{Zn}^{2+}$ ,  $\text{Ca}^{2+}$ , and  $\text{Ba}^{2+}$  bis(trifluoromethylsulfonyl)imide electrolytes from the dilute to the superconcentrated regime. No exchange phenomena occur within at least 100 ps, regardless of the ion identity, salt concentration, and presence of water. All of the observed spectral dynamics originate from the intermolecular energy transfer. These results place the lower experimental boundary on the ion–solvent residence times to several hundred picoseconds, much slower than previously suggested. With the help of MD simulations and conductivity measurements on the  $\text{Li}^+$  and  $\text{Zn}^{2+}$  systems, we discuss these results as a continuum of vehicular and structural modalities that vary with concentration and emphasize the importance of collective electrolyte motions to ion transport. These results hold broadly applicable to many battery-relevant ions and solvents.



## INTRODUCTION

Global climate change induced by greenhouse gases requires a decoupling of emissions and economic growth via utilization of the practically limitless solar- and wind-powered clean energy sources.<sup>1</sup> Daily and seasonal periodicity and weather fluctuations require effective means of grid energy storage for later use.<sup>2</sup> The increase of electric vehicles,<sup>3</sup> the explosive growth and ubiquity of mobile gadgets, drones, and wearable electronics rely on portable energy sources.<sup>4</sup> Metal-ion batteries represent one of the most popular and promising solutions to both these tasks, with Li-ion batteries currently being at the cutting edge of the commercially available technologies.<sup>5,6</sup> However, the need for higher energy density, improved safety, faster charging rate, longer cycle and calendar lives, and lower cost dictates the efforts for the development of novel ever more efficient battery chemistries.<sup>7,8</sup>

New electrolyte formulations emerge as a crucial part of these efforts. Innovative concepts have been put to use in recent years, such as advancement beyond lithium toward multivalent cations,<sup>9</sup> superconcentration, and utilization of unconventional solvents.<sup>8</sup> Magnesium,<sup>10</sup> calcium,<sup>11</sup> and zinc<sup>12</sup> ions are among the most promising and widely researched candidates since their double charge leads to higher volumetric energy density and high cell voltages. Given the added

advantages of being earth-abundant and having low cost and low toxicity, they have significant potential to replace lithium as charge carriers in batteries. Different ions may be superior in specific applications: for example, aqueous  $\text{Zn}^{2+}$  holds great promise for large-scale grid energy storage.<sup>13</sup>

Superconcentration exploits the unconventional regime characterized by the presence of solute ions in numbers comparable to solvent molecules in solution.<sup>14</sup> Contrary to the traditional 1 M concentration paradigm, dwelling on the regime of the maximum overall solution conductivity in nonaqueous electrolyte formulations, in superconcentrated electrolytes, the conductivity is lower, but the apparent lithium transference numbers are higher leading to smaller concentration polarization within the cell.<sup>15,16</sup> Significant expansion of the solvent electrochemical window can be achieved as a result of the anion-derived solid–electrolyte interphase that forms a kinetic barrier on the electrode and prevents the solvent from

Received: January 5, 2022

Published: April 26, 2022



participating in parasitic redox and intercalation processes that are often at the core of the cell degradation.<sup>17–19</sup> Superconcentration opens the way for solvents that were previously unimaginable as a solvating medium in batteries (e.g., water).<sup>20</sup> The expanded solvent choice allows for a fine tuning of the strength and topology of the cation–solvent interactions that determine the charging/discharging behavior at the electrodes.

On the other hand, superconcentrated electrolyte solutions are orders of magnitude more viscous than the respective neat solvents, and their microscopic structure is thought to be highly aggregated, consisting of percolated interconnected ion and solvent networks with metal ions being at the core and coordinated to both the anions and solvent molecules.<sup>21–23</sup> The charge transport by the conventional vehicular diffusion of solvated metal ions moving together with their solvent shells has been called into question in these systems. Instead, the ion hopping hypothesis that explains charge transport by the correlated hops of cations through a series of sequential shifts between various possible configurations of multidentate ligation to solvent and counterion has been suggested.<sup>24</sup> This mechanism is inspired by ion migration in the so-called single-ion electrolytes,<sup>25</sup> such as in solid-state<sup>26</sup> or lithium-ion polymer batteries,<sup>27</sup> and has been suggested based on molecular dynamics (MD) simulations,<sup>21,28–33</sup> but the direct experimental verification is missing. Pulsed-field gradient NMR experiments provided evidence of the unusually fast diffusion of Li<sup>+</sup> ions in relation to all other components,<sup>22,32–34</sup> but they typically cannot differentiate cations in various environments or bound versus free solvent/anions and thus measure the average diffusion across all of the species of a given nucleus in solution. Fast spin–lattice relaxation rates prevent reliable measurements on the nuclei of many divalent cations. Walden plots suggest that the ionic conductivity is decoupled from viscosity in these systems, casting doubt on the validity of the Stokes–Einstein relation,<sup>14,28,35,36</sup> but the real-time observation of ionic transport through a series of chemical exchanges remains extremely challenging.

Experiments must differentiate between various ionic and solvent structures and possess the necessary time resolution to track the ion hopping events that can be as fast as several picoseconds according to the simulations. Ultrafast two-dimensional infrared (2D IR) spectroscopy is a structurally sensitive method that is well suited to track the ultrafast chemical exchange events in electrolytes on a picosecond time scale.<sup>37–41</sup> It has been increasingly applied in recent years to the problems in the field of battery electrolytes.<sup>42–50</sup> Notably, it was used to explore the structural dynamics of dilute LiPF<sub>6</sub> solutions in battery-related organic carbonates by monitoring the carbonyl stretch modes of the solvent itself without introducing an extrinsic IR probe molecule that can perturb the solution structure.<sup>42</sup> These experiments demonstrated the growth of cross-peaks between the IR resonances of lithium-bound and free carbonates within several picoseconds that was interpreted as chemical exchange phenomena related to the macroscopic cation mobility in lithium-ion batteries. These results, corroborated by MD simulations,<sup>49</sup> painted a picture of highly dynamic Li<sup>+</sup> solvation sheaths being fluxional on the fastest time scales. Subsequent works focused on several Li electrolytes in a few solvents using similar computational and 2D IR approaches.<sup>40,46–48,50–55</sup> However, dynamic cross-peaks in two-dimensional spectroscopy can arise not only from the chemical exchange phenomena related to the solvation/desolvation events associated with ion hopping and eventually

related to charge transport but also from vibrational energy-transfer (VET) processes<sup>56</sup> that contribute to the same spectral signature and can be considered parasitic in the current context as they are unrelated to the ion desolvation and translocation.

Here, we adopt a probe-free approach by monitoring the solvent local vibration with femtosecond 2D IR spectroscopy to elucidate the structural dynamics of a series of battery electrolytes featuring various cations in acetonitrile: from classic Li<sup>+</sup> to multivalent Mg<sup>2+</sup>, Ca<sup>2+</sup>, Zn<sup>2+</sup>, as well as complementary Ba<sup>2+</sup> and K<sup>+</sup>. We use a mixture of solvent isotopologues to directly and unambiguously differentiate chemical exchange versus energy-transfer phenomena in all of the electrolytes in a full range of possible concentrations from the dilute to the superconcentrated regime. Regardless of the ion identity, electrolyte concentration, and water admixture content, no ultrafast chemical exchange phenomena are observed in these electrolytes within the broad 100 fs–100 ps time range. Instead, intermolecular energy-transfer processes dominate the spectral dynamics. These results put a lower bound for the solvent residence times around the cations to at least a few hundred picoseconds, rendering the solvent fluxional exchanges 1–2 orders of magnitude slower than previously claimed. This carries repercussions for the charge carrier diffusion length scales and transport mechanisms in these systems. While these conclusions are experimentally demonstrated here to be universally applicable for a variety of battery-relevant ions across a full range of concentrations, they are also expected to hold broadly not only for acetonitrile but for the majority of organic solvents due to their higher donicity (Gutmann donor number)—an empirical measure of the electron-donating ability and Lewis basicity of a coordinating nucleophilic solvent.<sup>57</sup> This parameter is of utmost importance in battery electrolytes as it determines the strength of the cation–solvent interactions that underlies the sluggish solvent exchange kinetics on these fast time scales.

## RESULTS

M(TFSI)<sub>*n*</sub> salts in acetonitrile (ACN) are used as electrolytes in the current work. M<sup>*n+*</sup> represents a series of cations of increasing charge densities (K<sup>+</sup>, Ba<sup>2+</sup>, Li<sup>+</sup>, Ca<sup>2+</sup>, Zn<sup>2+</sup>, Mg<sup>2+</sup>), and TFSI<sup>−</sup> is a bis(trifluoromethylsulfonyl)imide anion (Figure 1a). The cations were chosen to sample a large range of charge densities, including K<sup>+</sup> and Ba<sup>2+</sup> that offer an opportunity to sample charge densities lower than in the monovalent Li<sup>+</sup> system. TFSI salts have been attracting significant interest for the exploration of novel electrolyte formulations due to the noncoordinating nature of the bulky anion<sup>58</sup> and their exceptional solubility in a variety of solvents, opening the possibility to venture into the superconcentrated regime.<sup>17,18,59–61</sup> Acetonitrile was chosen as a solvent due to its excellent oxidative stability and compatibility with 5 V class cathodes, high dielectric constant, low viscosity, melting point, and price, as well as moderate toxicity that makes it a promising choice for the new generation of battery electrolytes. The poor reductive stability that in the past precluded the utilization of nitriles in batteries can be overcome in the superconcentrated regime due to the formation of the protective layer of the anion-derived interphase on the anode<sup>18</sup> and prevents corrosion of the current collector.<sup>35,62</sup> Acetonitrile features a prominent local C≡N vibrational mode that can be monitored with IR spectroscopy to obtain information about the structure and dynamics of these electrolyte solutions from the solvent's perspective.<sup>39,63,64</sup> We

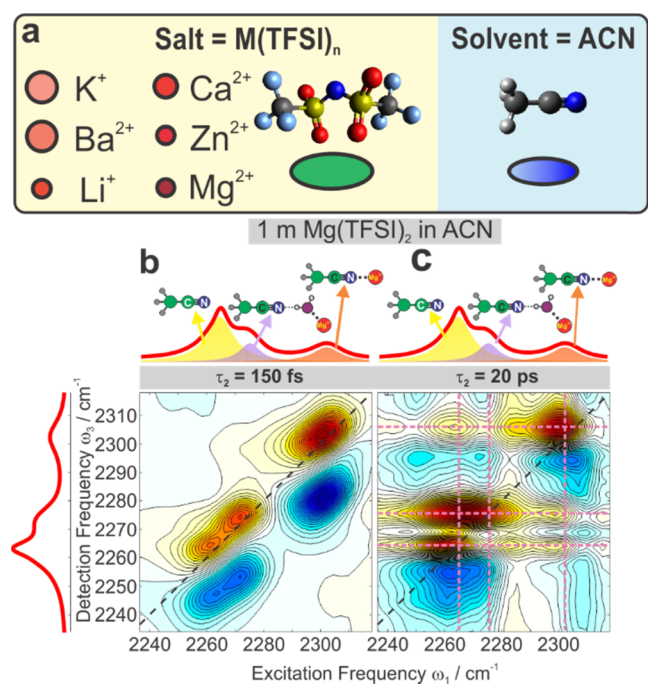


**Figure 1.** Acetonitrile electrolytes and representative 2D IR spectra in the solvent C≡N stretch region. (a) Schematic depiction of the components in electrolyte systems. Color shading of the cation reflects the increasing charge density, whereas the circle size is proportional to the ionic radius. (b, c) 2D IR spectroscopy of solvent in 1 m Mg(TFSI)<sub>2</sub> electrolyte in CD<sub>3</sub>CN at (b) an early waiting time of 150 fs and (c) a late time of 20 ps. Water admixture is present due to the highly hygroscopic nature of the Mg salt. Linear IR spectrum (red line, top and left) with the decompositions into contributions from different bands is shown on top. Cartoons illustrate the species responsible for each peak. Both diagonal and cross-peaks take the form of vertically displaced positive/negative doublets.

have shown previously that the solvent C≡N stretch is a sensitive marker for cation–solvent interactions in electrolytes since the metal-coordinated nitrile appears as a distinct band at frequencies higher than the free solvent, and the splitting between the two bands is determined by the cation charge density and solvent donicity.<sup>65</sup>

Stationary IR spectroscopy does not provide information on the dynamical interconversion of various species. Instead, ultrafast 2D IR spreads the infrared spectrum along the two axes that allows one to correlate the response at a detection frequency  $\omega_3$  upon excitation of a vibration at  $\omega_1$  as a function of waiting time  $\tau_2$  between the excitation and detection events. The spectral separation of the cation-bound and unbound nitriles makes possible to perform 2D IR spectroscopy where one can target the cross-peaks between these bands, and their growth dynamics with waiting time should directly report on the interconversion between these species.<sup>38</sup>

Figure 1b shows the 2D IR spectrum of Mg(TFSI)<sub>2</sub> in CD<sub>3</sub>CN at an early waiting time of  $\tau_2 = 150$  fs. The spectrum features three peaks (doublets) on the diagonal with a characteristic C≡N stretch frequency that arises from different acetonitrile species: the free CD<sub>3</sub>CN of bulk solution (2262 cm<sup>-1</sup>), a Mg<sup>2+</sup>-coordinated CD<sub>3</sub>CN (2305 cm<sup>-1</sup>), and a water-separated Mg<sup>2+</sup>–CD<sub>3</sub>CN pair, where acetonitrile makes a hydrogen bond to the water molecule that is coordinated to the metal cation (2274 cm<sup>-1</sup>).<sup>65</sup> The presence of this water-mediated species in a nominally nonaqueous electrolyte

solution originates from the high hygroscopicity of the Mg<sup>2+</sup> salt. Since water admixture is a deleterious nuisance in nonaqueous battery electrolytes, this spectral feature provides a useful and sensitive means for its detection. In contrast, at a longer waiting time of 20 ps, cross-peaks between all three species appear in the spectrum (Figure 1c). Strictly speaking, the cross-peaks monitor the fate of the initial mode-specific vibrational excitation during the waiting time. They can be interpreted as arising from the ultrafast interconversion between species, which changes the frequency of the excited bond, i.e., the dynamics of the solvent exchange.<sup>42</sup> However, they can also arise from the intermolecular vibrational energy transfer between different acetonitrile species, that is, the vibrational energy initially deposited in one nitrile stretching vibration migrates through space to another. The dichotomy of exchange versus energy transfer in 2D IR cross-peaks must be addressed. Monitoring the spectral dynamics of the solvent is necessarily complicated by the high abundance of solvent molecules at all salt concentrations (Table S1). Even in the most superconcentrated solutions, where there is about 0.7 ACN molecule/ion, the solvent concentration is at least 4.5 M. The average separation between nitriles is small, favoring energy transfer that steeply depends on distance.<sup>56</sup> A typical mitigation strategy to prevent VET via keeping the vibrational reporter at low concentration is obviously not possible in solvent-probing experiments. To differentiate between solvent exchange and energy transfer, it is necessary to monitor the cross-peaks between the species that cannot interconvert one into another but only exchange energy.

With that in mind, we use mixtures of the spectroscopically distinct acetonitrile isotopologues: CD<sub>3</sub>CN (A) and isotope-labeled CD<sub>3</sub><sup>13</sup>CN (L) to distinguish two solvent molecules within the same environment. This strategy does not introduce additives to solution beyond the species that are already present and thus avoids any perturbation of the solution morphology and dynamics. Employing the labeled CD<sub>3</sub><sup>13</sup>CN in mixture with CD<sub>3</sub>CN, we aim to separate intermolecular energy-transfer processes that are selectively encoded in the cross-peaks between the CD<sub>3</sub>CN solvent and the label. Without any salt, the <sup>13</sup>C-induced red shift of the C≡N stretch to 2224 cm<sup>-1</sup> in L gives rise to the intensity gain of the dark C–D stretch transition that appears at 2198 cm<sup>-1</sup> due to the coupling between these two modes (Figure 2a).<sup>65</sup> Interaction of highly polarizing metal cations with L leads to the emergence of a metal-coordinated <sup>13</sup>C≡N stretch at higher frequencies analogously to CD<sub>3</sub>CN and perturbs the coupling to the C–D (Figure 2a,b).<sup>65</sup>

We use a 1:1 volumetric mixture of the isotopologues as a solvent. The low-frequency half of the spectrum reports on L (pink), and the high-frequency half reports on A (green). Addition of salts to this mix results in the superposition of the spectra of the individual isotopologues, where all of the species can be unambiguously identified and their IR bands assigned (Figure 2). Using this mixture, we can spectrally differentiate the coordinated acetonitriles within a solvation shell of the metal ion (peaks L<sub>1</sub><sup>C</sup>/L<sub>2</sub><sup>C</sup> versus A<sup>C</sup>) as well as different noncoordinated nitriles (L<sub>1</sub>/L<sub>2</sub> versus A), in addition to coordinated versus uncoordinated solvent molecules (L<sub>1</sub>/L<sub>2</sub> versus L<sub>1</sub><sup>C</sup>/L<sub>2</sub><sup>C</sup>, A versus A<sup>C</sup>).

First, we apply femtosecond 2D IR spectroscopy to the mixture of two solvents in the absence of salts. Figure 3 shows the 2D IR spectrum of a solvent mixture at the early waiting time  $\tau_2 = 150$  fs. A square pattern of peaks L1–L4 belongs to

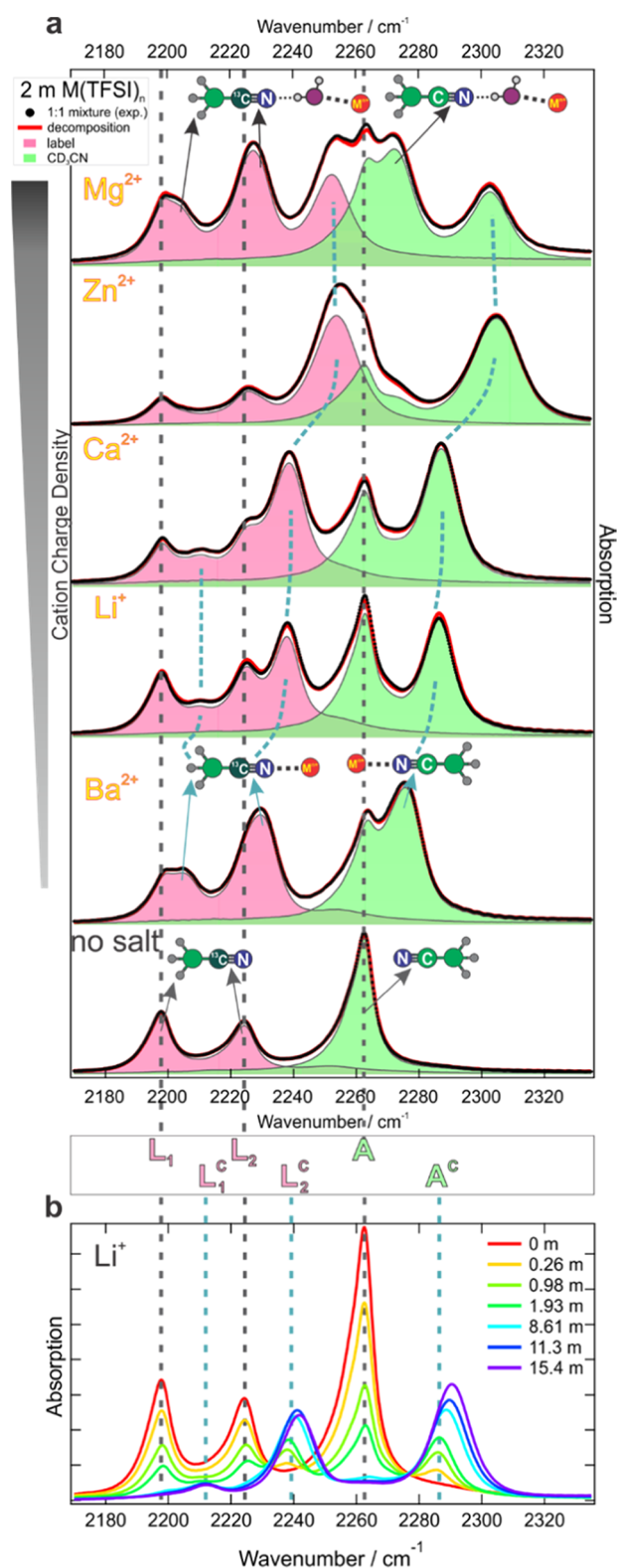


**Figure 2.** Linear IR spectroscopy of electrolytes in a mixture of acetonitrile isotopologues. (a) IR spectra of 2 m  $M(TFSI)_n$  solutions in a 1:1 mixture of  $CD_3CN$  (A, green) and  $CD_3^{13}CN$  labels (L, pink) for various  $M^{n+}$ . Cartoons represent species and their vibrations responsible for various peaks. All spectra are normalized to the common symmetric C–D stretch band at  $2116\text{ cm}^{-1}$ . (b) IR spectral changes upon increasing the concentration of LiTFSI. Metal-coordinated nitrile bands are designated with  $^c$ , and bands of the label are numerated ( $_1$  for C–D,  $_2$  for  $C\equiv N$  stretches).

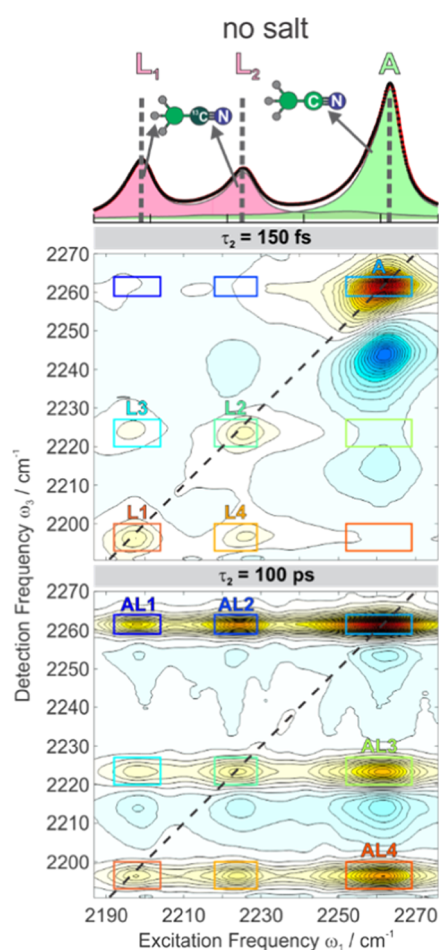


**Figure 3.** 2D IR spectroscopy of the 1:1 mixture of A and L acetonitriles at the early  $\tau_2 = 150\text{ fs}$  and late  $\tau_2 = 100\text{ ps}$ . Rectangles and labels designate bleaches of the various peaks. Linear spectrum is shown on top and decomposed into the contribution of L (pink) and A (green). Cartoons represent species and their vibrations responsible for various peaks.

the label, and the presence of the cross-peaks L3 and L4 is due to the strong intramolecular coupling between the C–D and  $^{13}C\equiv N$  stretch vibrations. The diagonal peak A comes from  $CD_3CN$ . At this early time, no cross-peaks between the vibrations of A and L (AL1–AL4) are visible, as expected for two weakly interacting acetonitrile isotopologues. In contrast, the 2D IR spectrum obtained at the longest waiting time of 100 ps reveals strong cross-peaks between all resonances, including prominent peaks AL1–AL4 (Figure 3). These peaks necessarily arise from vibrational energy transfer between molecules.

The amplitudes of the diagonal peaks decrease with increasing waiting time due to the vibrational relaxation depopulating the excited marker modes (Figure 4a). Typically, vibrational relaxation and re-equilibration in polyatomic molecules occur within a few picoseconds, which determine and ultimately limit the temporal window for 2D IR probing. However, for liquid acetonitrile, this process is remarkably slow.<sup>66,67</sup> Although the  $C\equiv N$  stretch relaxes with a short vibrational lifetime of 2–5 ps (Figure 4a and Table S4), this energy flows to the low-frequency C–C $\equiv$ N bending mode at  $\sim 369\text{ cm}^{-1}$  and results in a few  $cm^{-1}$  red shift of the  $C\equiv N$  stretch frequency.<sup>68,69</sup> This locally excited “hot” ground state

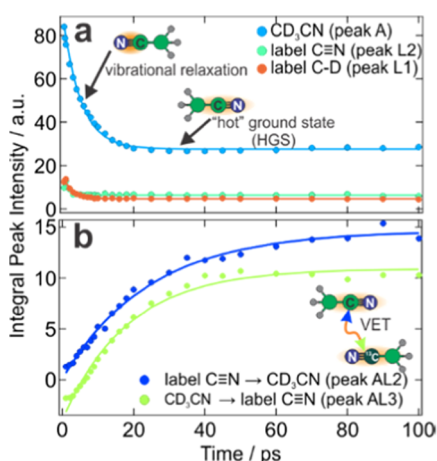


**Figure 4.** Dynamics of the various peaks in the 2D IR spectra of the 1:1 mixture of acetonitrile isotopologues. (a) Population relaxation dynamics of the diagonal bands demonstrates the vibrational relaxation of the initially excited C≡N to the local hot ground state. (b) Intermolecular vibrational energy transfer between acetonitrile molecules demonstrated via the growth of the cross-peaks AL2–AL3 that represent the same process proceeding in the opposite directions (shown schematically in the cartoon).

(HGS) does not change within our 100 ps experimental window, providing a way to extend the temporal window beyond many lifetimes of the initially excited C≡N stretch.

To quantify the vibrational energy-transfer kinetics, we track the cross-peak intensity as a function of waiting time. The conditional probability  $P$  that species  $\alpha$  transferred its vibrational energy to species  $\beta$  during the waiting time is obtained from the ratio of the integrated cross-peak intensity to the geometrical mean of the corresponding diagonal peaks

$$P = I_{\text{cross}}^{\alpha\beta} / \sqrt{I_{\text{diag}}^{\alpha} I_{\text{diag}}^{\beta}} \quad (1)$$

which henceforth we refer to as the cross-peak intensity for brevity.<sup>42,70</sup>

Intermolecular energy transfer in the mixture of acetonitriles is observed to take place with a 22–25 ps exponential time constant (Figures 4b and S5 and Table S4), which is significantly slower than the C≡N vibrational relaxation (Figure 4a and Table S4). This confirms that the acetonitrile following C≡N relaxation remains intramolecularly “hot” and not delocalized among low-frequency motions of many molecules as is the case, for example, in water.<sup>71</sup> The growth of cross-peaks represents the intermolecular transport of energy between the hot ground states of the two isotopologues,

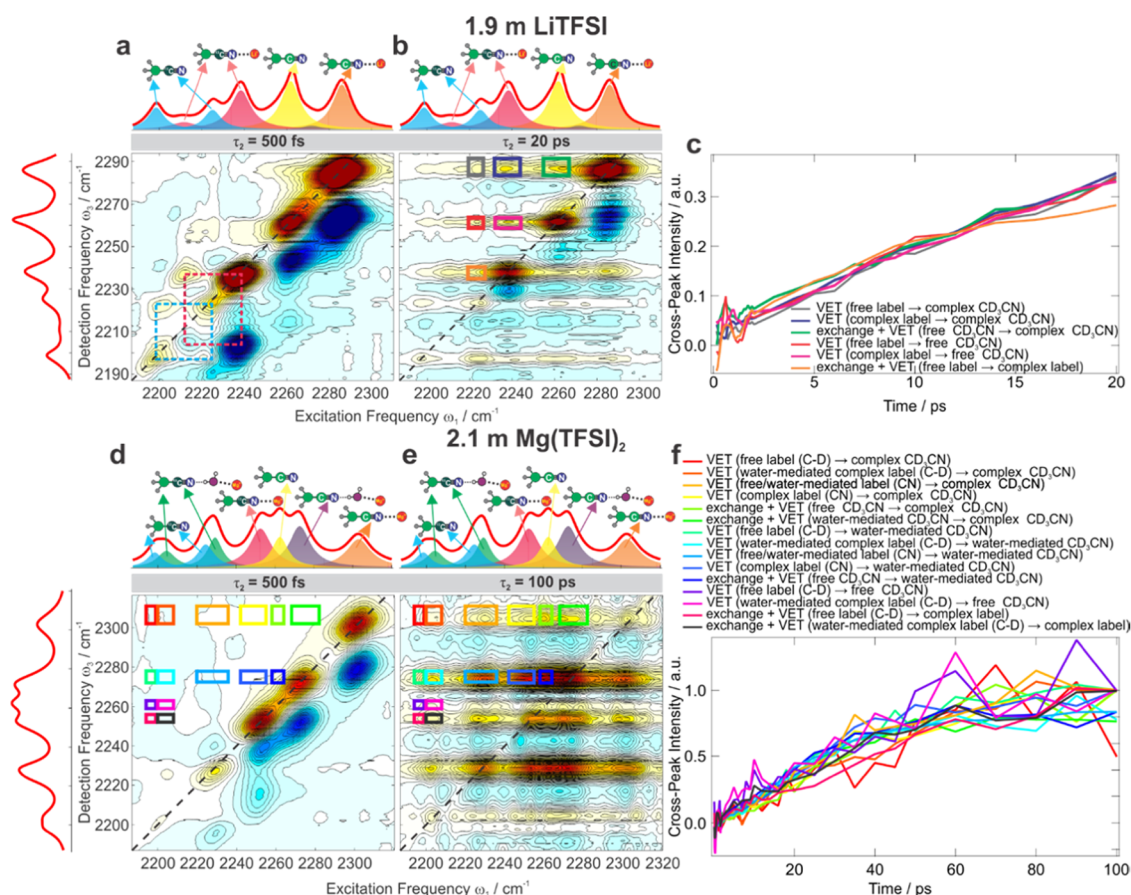


**Figure 5.** Separation of the chemical exchange and energy-transfer pathways. 2D IR spectroscopy of 1.9 m LiTFSI (a–c) and 2.1 m Mg(TFSI)<sub>2</sub> (d–f) in a 1:1 mixture of the label and CD<sub>3</sub>CN: (a, d) At an early waiting time of 500 fs. Dashed rectangles denote the Fermi-like coupling between the C–D and C≡N modes of the free (cyan) and complexed (pink) labels. (b, e) At late waiting time (20 ps for Li, 100 ps for Mg). Colored solid rectangles designate integration regions to track the kinetics of various pathways. Intense peaks are saturated in the 2D plot to emphasize low-intensity features. (c, f) Kinetics of the integrated peaks shown in (b, e), respectively. Each pathway is explicated. Linear IR spectra (red line, top and left) with the decomposition into contributions from different species (cyan: free label; pink: complexed label; yellow: free ACN; orange: complexed ACN; purple: water-mediated metal complex) are shown for panels (a, b, d, e).

not resonant transfer between two nitriles, which are just spectators in this process, not the acting figures.

To unambiguously differentiate chemical exchange versus energy-transfer pathways, we subsequently applied 2D IR to the  $M(\text{TFSI})_n$  salts dissolved in the mixture of  $\text{CD}_3\text{CN}$  and  $\text{CD}_3^{13}\text{CN}$  acetonitriles. The cross-peaks between the resonances of two different isotopologues can arise only from intermolecular energy transfer, whereas cross-peaks between the bands of the same isotopologue can arise from both VET and chemical exchange processes.

Cross-peaks between the distinct ion-coordinated and free solvent resonances accessible via 2D IR spectroscopy are a direct and unambiguous way of measuring the change from one molecular configuration to another regardless of the fact that the mechanism of this change is the chemical exchange or energy transfer.<sup>56,72,73</sup> More common spectral diffusion measurements of the vibrational reporter can observe solvent exchange events between configurations;<sup>74–76</sup> however, this approach typically senses fast solvent fluctuations within one configuration. Additionally, this approach does not allow for a separation of chemical exchange and energy-transfer phenomena that would both contribute to spectral diffusion.<sup>77,78</sup>

Figure 5a demonstrates the exemplary spectrum of 1.9 m LiTFSI at an early waiting time of 500 fs. Each of the six peaks seen in the linear IR spectrum appears on the diagonal, but cross-peaks are present only between the intramolecularly coupled C–D and  $\text{C}\equiv\text{N}$  modes of the free label and between the same modes of the coordinated label. However, at this early time, no intermolecular cross-peaks are observed.

The intermolecular cross-peaks signifying chemical exchange and energy transfer grow in with waiting time and appear prominently at 20 ps (colored rectangles; Figure 5b). Whereas there are many cross-peaks present in the spectrum, we focus only on the cross-peaks between  $\text{C}\equiv\text{N}$  features in the upper left corner above the diagonal. The cross-peaks in the lower right corner symmetric across the diagonal bear identical information, but their analysis is more complicated due to the overlapping excited-state  $|1\rangle \rightarrow |2\rangle$  absorption features that appear below the diagonal bleaches in the 2D IR spectrum (Figure S9). The green rectangle in Figure 5b indicates the cross-peak that represents both chemical exchange and the energy transfer between the free and coordinated  $\text{CD}_3\text{CN}$ . The orange rectangle represents the same pathways but for the label. In contrast, the other four rectangles are purely energy-transfer cross-peaks between  $\text{CD}_3\text{CN}$  and  $\text{CD}_3^{13}\text{CN}$  in free and coordinated forms in various combinations (e.g., the red rectangle represents VET between free nitriles, whereas the gray one is between the free label and coordinated  $\text{CD}_3\text{CN}$ ). The navy rectangle encodes the energy transfer between the coordinated A and L isotopologues that can occur either between acetonitriles coordinated to the same cation within a single solvation shell or between nitriles in the solvation shells of two different cations. Tracking the evolution of these cross-peaks with waiting time allows us to quantify directly the dynamics of the underlying processes. Figure 5c shows the experimental kinetic traces for all six cross-peaks in Figure 5b in the initial rate regime. Clearly, all of the cross-peaks follow the same dynamics regardless of their specific nature. This finding indicates that the combination of the chemical exchange and VET pathways has the same kinetics as the VET pathway alone. It implies that chemical exchange surprisingly does not contribute within the 20 ps time window in this sample.

The same analysis was performed for other concentrations of LiTFSI from dilute 0.25 m to superconcentrated 15.4 m (Figures S6–S11). In all of the samples, we obtained the identical result: all of the cross-peaks manifest the same dynamics with no contribution of chemical exchange phenomena independent of the Li salt concentration despite the changes in the  $\text{Li}^+$  solvation structures.<sup>79</sup>

To find out whether this behavior is specific to Li electrolytes, we turned to other  $M(\text{TFSI})_n$  salts with varying cation charge densities:  $\text{Mg}(\text{TFSI})_2$ ,  $\text{Zn}(\text{TFSI})_2$ ,  $\text{Ca}(\text{TFSI})_2$ , and  $\text{Ba}(\text{TFSI})_2$  investigating the same concentration range from 0.25 m to the highest practically achievable concentration, which varied for each salt but was invariably in the superconcentrated regime (Table S1). Figure 5d demonstrates how the complex linear spectrum (shown as a red line) of a divalent  $\text{Mg}^{2+}$  system featuring multiple overlapping peaks from various species is deconvoluted in 2D IR. We focus on only some of the numerous cross-peaks that appear with increasing waiting time in Figure 5e, whose kinetics are shown in Figure 5f, and more data are presented in Figures S14 and S15. We follow their dynamic evolution over the entire 100 ps time window until they reach their maximum possible intensity. Despite its enormous apparent complexity due to featuring a multitude of pathways and processes, Figure 5f clearly shows that there is no difference in the dynamical evolution of any of the cross-peaks regardless of the nature of the underlying process and they all fall on the same curve. This is a general observation that we consistently found for all of the salts at all concentrations (Figures S6–S27). The identical temporal evolution of all of the cross-peaks indicates that no chemical exchange is operative on this time scale, and the apparent spectral dynamics stem entirely from energy transfer. Even in the case of  $\text{Ba}^{2+}$  featuring the lowest charge density that still induces spectral splitting of the  $\text{C}\equiv\text{N}$  stretch band, the exchange time scale is too long to be observed on top of the energy transfer.  $\text{K}^+$  has even lower charge density but its solubility in ACN as a TFSI<sup>−</sup> salt is very low and it does not cause appearance of a distinct ion-coordinated band, making these experiments impossible.

The salts with the most polarizing ions ( $\text{Zn}^{2+}$  and  $\text{Mg}^{2+}$ ) are highly hygroscopic and contain some amount of water impurity. This leads to the appearance of the additional peaks of water-separated  $\text{Zn}^{2+}/\text{Mg}^{2+}$  ACN pair in their spectra (Figures 2a and 5d,e), as discussed previously.<sup>65</sup> The water admixture, although a nuisance for electrochemistry, is an additional useful variable in our experiments. A recent study on the influence of water content in LiTFSI–ACN electrolytes of various concentrations pointed out that even at 1200 ppm water admixture, the physicochemical properties of solutions remain intact, and only the electrochemical window shrinks.<sup>80</sup> Therefore, although it does not significantly perturb the macroscopic properties of the solutions, it could potentially affect the microscopic exchange dynamics. Additionally, the formation of the water-mediated  $\text{Zn}^{2+}/\text{Mg}^{2+}$ –ACN pairs provides an opportunity to reveal whether the exchange dynamics differs when an acetonitrile molecule is displaced from the first solvation shell of the cation by water molecules. We have tracked the kinetics of the cross-peaks between the water-mediated and free/coordinated ACN species in  $\text{Mg}(\text{TFSI})_2$  and  $\text{Zn}(\text{TFSI})_2$  systems that follow the exchange of the second-shell solvent molecules. We found no difference in their temporal evolution from all other cross-peaks. This indicates that at least in the case of divalent cations even the

second-shell solvent molecules are tightly coordinated and do not exchange within 100 ps. It also points out to the dominance of the VET over all of the species in solution (Figures S12–S22).

Lastly, we compared how the cation identity and concentration affect the energy-transfer time scale, finding no significant concentration dependence and only a modest dependence on cation. For example, in all  $\text{Zn}^{2+}$  solutions, VET between two types of coordinated ACN occurs on  $\sim 30$  ps time scale (Figure 6), whereas in the case of  $\text{Mg}^{2+}$ , it takes

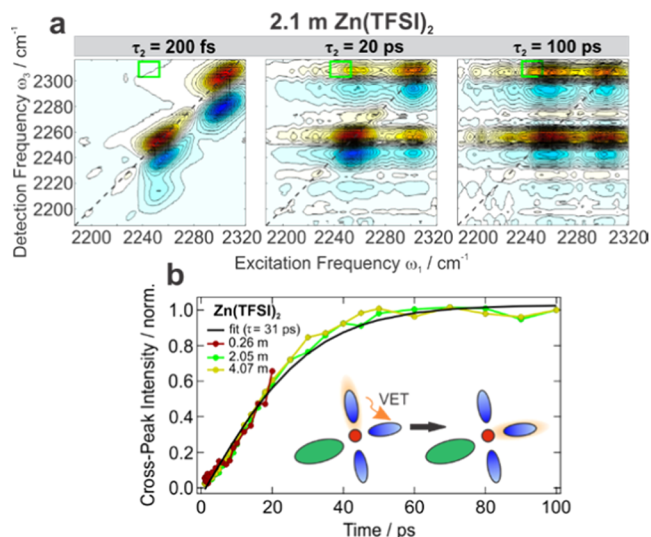


**Figure 6.** Concentration dependence of the energy-transfer rate. (a) 2D IR spectra of  $\sim 2$  M  $\text{Zn}(\text{TFSI})_2$  at three representative waiting times, highlighting the energy-transfer cross-peak between two coordinated acetonitrile isotopologues. (b) Energy-transfer dynamics in  $\text{Zn}(\text{TFSI})_2$  electrolytes at various concentrations. The cartoon shows the scheme of the underlying VET process between the coordinated ACNs within the same solvation shell.

$\sim 50$  ps (Section S2.2.3 and Table S5). The VET occurs similarly in all solutions and is slower than 25 ps in the absence of salts. These observed several tens of ps time scales of energy-transfer limit our ability to ascertain the value of a much slower solvent exchange rate. Assuming the mechanism, in which both processes are independent of each other, the cross-peaks grow with the sum of the rates, and kinetics of the faster VET process impose the stringent limitation on our ability to differentiate slower processes. For example, with our current signal-to-noise ratio, we find that the exchange rate is not faster than  $\sim 400$ – $500$  ps in the case of  $\text{Mg}^{2+}$  and  $\sim 250$  ps for  $\text{Zn}^{2+}$  (Figures S30 and S31). These values can serve only as the lower boundary of the experimentally determined solvent exchange time scale in these divalent cation systems because the slower processes become indistinguishable on top of the VET. The concentration independence of the VET rate for a given cation suggests that it represents energy hopping between solvent molecules within the same solvation shell (Figure 6b). On the other hand, the equivalence of the VET kinetics across all of the cross-peaks for a given system indicates that the solution structure is tightly packed and aggregated. In such a solution, various species are blended together to form the interconnected network and similar distances separate solvent molecules that are free, ion-coordinated, or surrounded by anions. No substantial differ-

ence in the rates of various energy-transfer pathways means that on average there is a similar probability of an excited acetonitrile to transfer energy to its neighbor regardless of whether they are both coordinated to the same or different cations or whether they are metal-coordinated at all.

To access ion transport properties, we measured the ionic conductivity  $\sigma$  for  $\text{LiTFSI}$  and  $\text{Zn}(\text{TFSI})_2$  acetonitrile systems as a function of concentration (Figure 7a). In the dilute

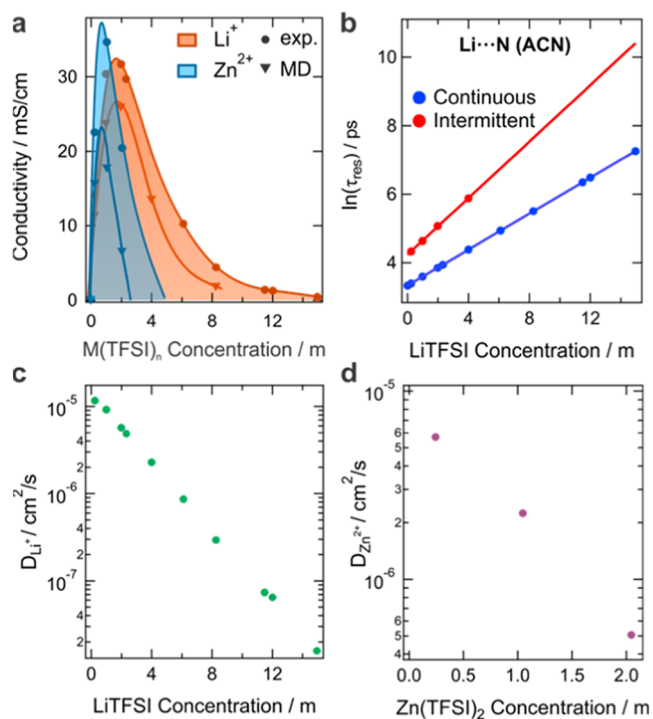


**Figure 7.** Transport phenomena and MD simulations. (a) Experimental (circles) and MD simulated (triangles) ionic conductivities of monovalent  $\text{Li}^+$  (orange) and divalent  $\text{Zn}^{2+}$  (blue) ACN electrolytes as a function of salt concentration. Lines are spline fits. (b) Continuous (blue) and intermittent (red) solvent residence times near the  $\text{Li}^+$  cation as a function of salt concentration computed from MD simulations. Exponential fits are shown as the respectively colored lines on the logarithmic vertical axis. (c, d) Diffusion coefficients obtained from the experimental conductivity accounting for the inverse Haven's ratio calculated from MD simulations as a function of concentration in  $\text{M}(\text{TFSI})_n$ –ACN systems for  $\text{Li}^+$  (c) and  $\text{Zn}^{2+}$  (d).

regime, the conductivity increases with concentration due to the increasing number of charge carriers, reaching a maximum around the classical 1 M regime (1–2 m), and then decreases with concentration due to the ion aggregation phenomena and the increase of the viscosity. Both  $\text{Li}^+$  and  $\text{Zn}^{2+}$  systems display large maximum conductivities of  $>30$  mS/cm (consistent with ref 21) that make them some of the most conducting nonaqueous electrolytes. In the superconcentrated regime, the conductivity drops to  $<1$  mS/cm for both.

The predictions we make about the molecular-scale solvation dynamics that govern cation transport can be compared to the macroscopic conductivity with the help of classical MD simulations (Section S1.2.4). Figure 7a shows that they reproduce the experimental values very well, correctly predicting the shape and peak of the conductivity concentration dependence. Additionally, the simulations quantitatively match the apparent  $\text{Li}^+$  transference numbers available

from ref 21 (Figure S37b). The quality of these comparisons gives us confidence that the simulations describe the microscopic dynamics as well. On that basis, we computed residence autocorrelation functions for  $\text{Li}^+$  ions coordinated with acetonitrile using two criteria: intermittent and continuous residence. The difference between these correlation functions is whether the  $\text{Li}^+$ –ACN contact is allowed to break and reform (intermittent) or must be sustained at all times (continuous) so that the residence is maintained (Section S3). The solvent residence times ( $\tau_{\text{res}}$ ) around the cations were obtained by integrating the respective functions (Section S3 and Figures S36, S42, and S43). Chemical exchange cross-peaks in a 2D IR experiment report on the intermittent residence, which is always longer than its continuous counterpart. We find that in accord with the experimental observations, the intermittent residence times for  $\text{Li}^+$  are >100 ps in the 1 m regime and they increase exponentially with concentration reaching 33 ns for the 15 m system (Figure 7b). The exponential scaling of residence times with concentration is a general phenomenon that we observe for both  $\text{Li}^+$ –solvent and  $\text{Li}^+$ –anion interactions in ACN (Figure S39), as well as that found in water,<sup>81</sup> organic carbonates,<sup>82</sup> and other systems. This scaling is practically useful because it allows us to predict the intermittent residence times for the most concentrated systems where the transport is very slow and the respective correlation function does not decay appreciably within tens of nanoseconds, making the calculation of transport properties via MD simulations impractical.

We extracted experimental diffusion coefficients of  $\text{Li}^+$  ion ( $D_+$ ) from the conductivity measurements by using the Nernst–Einstein equation

$$\Lambda_m = (\nu_+ z_+^2 D_+ + \nu_- z_-^2 D_-) \frac{F^2}{RT} \quad (2)$$

where  $+/-$  relates to the cation/anion,  $\Lambda_m$  is the molar conductivity,  $z$  is the charge,  $\nu$  is the number of ions per formula unit,  $F$  is Faraday's constant,  $R$  is the ideal gas constant, and  $T$  is temperature. The  $\text{Li}^+$  apparent transference numbers ( $D_+/(D_+ + D_-)$ ) of 0.5–0.6 were measured previously<sup>21</sup> for  $\text{LiTFSI}$ –ACN systems. However, the Nernst–Einstein relation does not account for ion–ion correlations and therefore holds poorly for highly concentrated electrolytes if used on the experimental  $\Lambda_m$  values directly. Instead, the inverse Haven's ratio ( $H^{-1}$ )

$$H^{-1} = \frac{\sigma}{\sigma_{\text{NE}}} \quad (3)$$

can be used to obtain the idealized Nernst–Einstein conductivity ( $\sigma_{\text{NE}}$ ) from the experimental results ( $\sigma$ ).

In our electrolytes, ion correlations cannot be neglected: the  $H^{-1}$  drops steeply from the unity at infinite dilution to 0.5–0.6 already at moderate concentrations of  $\text{Li}^+$  and decreases even more dramatically for  $\text{Zn}^{2+}$  (Figures S37a and S41a). Although our simulations tend to underestimate the absolute experimental conductivity values by up to a factor of  $\sim 2$  (Figure 7a), the ratio of the transport properties such as apparent transference numbers or the inverse Haven's ratio reproduces the experimental results quantitatively (Figure S37), likely due to the cancellation of errors. Therefore, we used the  $H^{-1}$  from MD simulations to determine the idealized Nernst–Einstein conductivity from the experimental results, from which by using the  $\text{Li}^+$  apparent transference numbers, we determine its

diffusion coefficient. The value of  $D_+$  is large and reaches  $10^{-5}$   $\text{cm}^2/\text{s}$  in the dilute regime but drops exponentially with concentration (Figure 7c). A similar approach can be used for the  $\text{Zn}$ –ACN system revealing  $\text{Zn}^{2+}$  diffusion coefficient (Figure 7d).

## DISCUSSION

Our 2D IR experiments on the mixture of solvent isotopologues allow for clear differentiation of chemical exchange versus vibrational energy-transfer phenomena in the solvation sheaths of a wide range of battery-relevant cations of various polarizing abilities ( $\text{Li}^+$ ,  $\text{Mg}^{2+}$ ,  $\text{Zn}^{2+}$ ,  $\text{Ca}^{2+}$ ,  $\text{Ba}^{2+}$ ) in acetonitrile. Surprisingly, chemical exchange phenomena are sluggish regardless of the cation identity or salt concentration across the entire possible range, and the experimentally determined lower boundary of solvent residence times around this broad selection of cations is at least several hundreds of ps. We argue below that these results are not unique to acetonitrile and pertain to a vast majority of battery-relevant organic solvents. The solvation and desolvation events are much slower than previously suggested, and the cation solvation shells are rather static and rigid rather than highly fluxional on the ultrafast time scale. Instead, the observed 2D IR spectral dynamics are dictated by the intermolecular energy transfer (Figure 8a). There are many possible mechanisms of intermolecular vibrational energy transfer that were reported in the literature over the years,<sup>86,83</sup> including those in which energy is transported via low-frequency modes.<sup>84,85</sup> Since deducing a molecular mechanism for this process is a significant challenge in itself, we do not attempt to address this in the present work. We emphasize that our results were obtained using the intrinsic solvent mode as a vibrational reporter without adding any extrinsic probe to avoid perturbation to the solution structure or morphology of these electrolytes. In the general case, it is exceedingly difficult to differentiate chemical exchange and energy transfer, and it is only possible here because the isotope-edited solvent mixture allows us to distinguish unimolecular and intermolecular processes.

Our results are in contrast to the previous report on the ultrafast fluxional exchange phenomena in  $\text{Li}^+$  solvation shells in organic carbonates by Lee et al.,<sup>42</sup> where the experimentally observed several ps growth of the cross-peaks between ion-coordinated and free carbonyl resonances was assigned to solvent chemical exchange phenomena. The authors in that case argued that intermolecular energy transfer between the free and coordinated solvents should accelerate upon the increase of salt concentration, and no such increase was observed. However, the validity of such reasoning depends on the mechanism of vibrational energy transport for which multiple processes can contribute. We performed the same analysis on the transient absorption data for our  $\text{Li}^+$  system analogously to Lee et al.<sup>42</sup> across a range of concentrations to show that the average vibrational relaxation rate of uncoordinated acetonitrile stays nearly the same despite the dominance of the intermolecular energy transfer (Section S2.2.4 and Table S6). Therefore, we assert that the only strictly reliable method of differentiating VET versus chemical exchange in a single solvent is via isotope labeling.

Another conclusion we reach here is the independence of chemical exchange processes on the presence and concentration of small amounts of water present as an admixture in these systems. Water forms a distinct water-mediated cation–

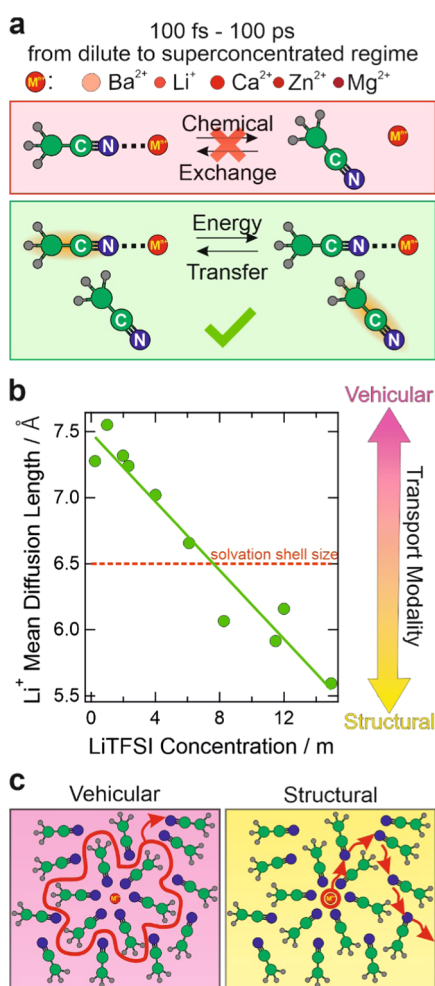


**Figure 8.** Chemical exchange-mediated charge transport. (a) Schematic representation of the processes behind dynamic cross-peaks in 2D IR spectra. (b) Li<sup>+</sup> root-mean-square diffusion distance  $\lambda_{\text{rms}}$  between solvent switching events compared with solvation shell radius (dashed red line). (c) Illustration of the extreme ends of the spectrum of transport modalities: pure vehicular and structural mechanisms of charge transport. The vehicles of translocating charge are shown in red. Red arrows depict charge transport.

acetonitrile pair, in which water coordinates to the metal ion that boosts the H-bond-donating ability, allowing it to form a strong H-bond to the nitrile making it spectroscopically distinguishable from both a directly coordinated and non-coordinated C≡N. The slow exchange in this water-separated species evidences that solvent chemical exchange around the divalent cations is too slow not only upon direct coordination but also at least in the second solvation shell. MD simulations of the solvent residence times in the second ACN solvation shell of Zn<sup>2+</sup> confirm this interpretation (Figure S43). Water does not accelerate exchange dynamics so that it could be observed here. It is interesting to contrast this result with the report on the lubrication effect of water on the motion of a molecular machine.<sup>86</sup> In that case, the presence of water significantly accelerated the rotation of a molecular wheel around an axle, the effect that was ascribed to the formation of a three-dimensional hydrogen bond network. In our case, the concentration of water is rather low and the formation of the bulk-like aqueous network does not occur in these electrolyte solutions.<sup>23</sup> It is also unlike in a recent communication<sup>87</sup> where

water admixture coordinating to the anions was reported to accelerate solvation dynamics in a deep eutectic solvent.

We relate the sluggish rate of the chemical exchange phenomena in acetonitrile solvation shells to the strong coordination between the cations and solvent molecules. By itself, acetonitrile is one of the fastest known dipolar solvents, where solvent motions occur on tens to a few hundred fs time scales; solvation upon photoexcitation is complete within 1 ps,<sup>88</sup> and full molecular reorientation takes 1.6 ps.<sup>89</sup> Around the strongly polarizing ions presented here, its motion is slowed down by several orders of magnitude, so that no molecular switching events are observed within a 100 ps observation time window. This temporal window is limited not by the vibrational relaxation rate of the C≡N but by the VET rate that determines when the energy transfer among acetonitrile molecules is complete.

Equipped with both the diffusivity and residence time values (Figure 7b–d), we could evaluate the root-mean-square cation diffusion length ( $\lambda_{\text{rms}} = \langle \lambda^2 \rangle^{1/2}$ ) between the solvent switching events using the Einstein–Smoluchowski equation based on the three-dimensional random walk

$$\lambda_{\text{rms}} = \sqrt{6D_+ \tau_{\text{res}}} \quad (4)$$

This approach is justified here since the switching of ion coordination state is slow on the time scale of solvent fluctuations.<sup>46</sup> The value of  $\lambda_{\text{rms}}$  provides an important metric to assess the modality of the Li<sup>+</sup> ion transport mechanism, and the independent evaluation of both the diffusion coefficient and residence times provides access to its concentration dependence (Figure 8b). This parameter decreases linearly from 7.5 Å in the dilute regime to 5.5 Å in the superconcentrated systems, providing evidence of the decreasing length scale for diffusive transport. These values of  $\lambda_{\text{rms}}$  can be compared to the cation solvation shell radius, which is estimated as 6.5 Å based on the ion–solvent interaction distance and acetonitrile molecular size (Section S4).<sup>82</sup>

Ion diffusion is often discussed in terms of two molecular mechanisms: structural diffusion, in which the cation does not appreciably diffuse together with its coordination shell but switches its solvent partners frequently, and vehicular diffusion, where the ion moves together with its solvating environment (Figure 8c). While these mechanisms do not relate in a simple manner to the electrolyte dynamics determining  $\lambda_{\text{rms}}$ , we believe the shortening of the Li<sup>+</sup> diffusion length with LiTFSI concentration can be interpreted as a shifting combination of ion transport modalities between these limits. When the Li<sup>+</sup> diffusion length is much larger than the size of its first solvation shell, vehicular diffusion involving collective electrolyte dynamics is the more likely explanation. On the other hand, short-range solvation shell desolvation and resolvation processes contributing to structural diffusion are expected when the Li<sup>+</sup> diffusion length scale is much smaller than the solvation sheath size, as we find in the superconcentrated regime. Given the relatively similar values of the diffusion length and shell size even in the most concentrated solution (5.5 versus 6.5 Å), which is still notably higher than the size of a single acetonitrile molecule (2.6 Å) or the Li<sup>+</sup>–ACN contact distance (2.2 Å; Figure S44), we consider this as an indication that the transport is a mixture of modalities rather than an exclusive occurrence of one of them. There can be several translocation mechanisms at play with different characteristic step sizes, and the increase in LiTFSI concentration reweights

the distribution of paths toward those with shorter diffusion length scales where cation changes solvent partners before diffusing with them over the length much larger than their size. We emphasize that this shift toward structural diffusion is achieved not via short residence times and ultrafast solvent switching events. Instead, the desolvation and resolvation events become ultraslow, but this decrease in solvent fluxional mobility around the ion is overshadowed by the drop in the importance of the vehicular mechanism due to the formation of the aggregated network of ions and solvent molecules that is behind the viscosity increase. As a result, the decline in vehicular mobility renders the structural mechanism relatively more important despite that in absolute terms it is also disfavored.

In contrast to  $\text{Li}^+$ , for  $\text{Zn}^{2+}$ , we could not obtain a reasonable estimate of the ion–solvent residence time even when the MD trajectory was extended to 120 ns, as the residence autocorrelation function does not decay appreciably on this time scale. This indicates that the  $\text{Zn}^{2+}$ –ACN residence times are dramatically longer than  $\text{Li}^+$ –ACN residence times, reaching the values of hundreds of ns even at low concentrations in accord with significantly stronger interaction with a smaller divalent ion. Given the diffusion coefficient calculated from MD simulations (Figure 7d and Section S3), taking the 100 ns value as a lower boundary of the residence time in the most dilute solution and assuming similar exponential scaling of the residence times with concentration, we could only put a lower boundary on the  $\text{Zn}^{2+}$  diffusion length scale. It is drastically longer than  $\text{Li}^+$  and spans at least several tens of nm in the dilute regime to at least several nm in the superconcentrated one (Section S3). These large length scales far exceed the  $\text{Zn}^{2+}$  solvation shell size of 5.8 Å (Section S4) and illustrate that highly collective, correlated motions involving cations, counterions, and acetonitrile need to be considered in any mechanism. As such, by focusing on the local solvation around any one ion, the discussion of vehicular and structural diffusion hides that these terms are proxies for dynamical processes of the electrolyte evolving over much longer correlation lengths.

Finally, although these results are obtained for acetonitrile as one of the newly considered candidates for the role of the cation-solvating media in metal-ion batteries,<sup>8</sup> they can likely be generalized to a broad selection of solvents beyond acetonitrile. We have demonstrated that the strength of ion–solvent coordination is at the core of the dramatic extension of solvent residence times, meaning that solvent donicity, which is a measure of the solvent coordinating power and Lewis basicity, is a key factor that governs such behavior from the solvent side. Out of various classic (cyclic and linear organic carbonates), revisited (ethers, THF, sulfolane), and unconventional (DMSO, phosphate esters and phosphamides, water) solvents that are currently explored for the use in novel ever more efficient battery electrolytes, acetonitrile is on the lower end of the donor number spectrum (Table S8). Its donicity is similar to sulfolane and carbonates, lower than in ethers, and significantly lower than in DMSO and phosphamides. This implies that even longer residence times and slower solvent exchange events are expected in those solvents. As a result, we believe that the absence of ultrafast (<100 ps) solvent exchange toward metal cations is rather universal and independent of the solvent identity across a broad range of donicities, and only significantly weaker coordinating solvents (e.g., fluorinated esters<sup>90</sup> or ethers<sup>91</sup>) can be reasonably

expected to undergo ps exchange events around these cations. It has been demonstrated that weakening ion–solvent interactions leads to the dramatic increase in battery electrolyte performance at extremely low temperatures.<sup>92</sup> Recent MD simulations of multivalent nonaqueous electrolytes point out that overcoming strong cation–solvent coordination is a major bottleneck limiting the performance of these systems, whereas the interactions with bulky noncoordinating anions can be beneficial for transport properties and processes at electrodes.<sup>93</sup> We envision that accelerated exchanges can be expected only in the extremely low-coordinating solvents to be able to contribute to the enhancement of ion transport properties. The conventional organic solvents feature not ultrafast but rather ultraslow chemical exchange dynamics with respect to the battery-relevant cations.

These experimentally determined bounds on the exchange rates serve as stringent limitations that could be used to validate future MD simulations that are often used to screen electrolyte properties, provide the microscopic structures of electrolyte formulations, or validate the proposed ion transport mechanisms. They will also serve as a reference point for future experiments aiming at elucidating the details of charge transport. The stability of a  $\text{Li}^+$  solvation sheath, its structure, and dynamics are central factors dictating the interfacial chemistry in Li-ion batteries. Therefore, these results also bear significance for the solvation and desolvation processes at electrode interfaces in novel types of metal-ion batteries. We therefore hope that these results will also prove useful for future studies of the solid–liquid and electrified interfaces for a broad range of charge carriers.

## CONCLUSIONS

2D IR experiments performed on the intrinsic  $\text{C}\equiv\text{N}$  stretch solvent vibrational mode of acetonitrile in a variety of electrolytes composed of cations with various charge densities ( $\text{K}^+$ ,  $\text{Ba}^{2+}$ ,  $\text{Li}^+$ ,  $\text{Ca}^{2+}$ ,  $\text{Zn}^{2+}$ ,  $\text{Mg}^{2+}$ ) and a  $\text{TFSI}^-$  anion across a full possible concentration range from the dilute to the superconcentrated regime demonstrate the absence of ultrafast chemical exchange phenomena within 100 ps. Breakage and formation of ion–solvent contacts can be estimated to take place on at least many hundreds of ps time scales regardless of the ion identity and concentration. Exchange in the second solvation shell is also slower than 100 ps. The apparent spectral dynamics manifested as a growth of cross-peaks on the picosecond time scale originates entirely from intermolecular vibrational energy transfer. The latter could be unambiguously differentiated from the exchange phenomena by employing a mixture of specially designed acetonitrile isotopologues. MD simulations confirm these experimental predictions and allow us to evaluate the range of possible values of ion–solvent residence times, which grow exponentially with salt concentration. As a result, the vehicular diffusion is a dominant charge transport mechanism in divalent electrolytes, but in  $\text{Li}^+$  systems, the charge transport occurs via a mixture of vehicular and structural diffusion with increasing importance of the structural component upon the increase of  $\text{Li}^+$  concentration. This behavior is not unique to acetonitrile but is expected to be universal for the majority of the nonaqueous battery solvents that have higher donicities that determine the strength of the ion–solvent coordination.

## ■ ASSOCIATED CONTENT

### SI Supporting Information

The Supporting Information is available free of charge at <https://pubs.acs.org/doi/10.1021/jacs.2c00154>.

Experimental details and methods, details of MD simulations, additional spectroscopic steady-state and time-resolved IR data, evaluation of transport phenomena and solvation shell size, description of solvent properties, supplementary references, Figures S1–S44, and Tables S1–S8 (PDF)

## ■ AUTHOR INFORMATION

### Corresponding Author

**Andrei Tokmakoff** – James Franck Institute, The University of Chicago, Chicago, Illinois 60637, United States; Department of Chemistry and Institute for Biophysical Dynamics, The University of Chicago, Chicago, Illinois 60637, United States; Joint Center for Energy Storage Research, Argonne National Laboratory, Lemont, Illinois 60439, United States; [orcid.org/0000-0002-2434-8744](https://orcid.org/0000-0002-2434-8744); Email: [tokmakoff@uchicago.edu](mailto:tokmakoff@uchicago.edu)

### Authors

**Bogdan Dereka** – James Franck Institute, The University of Chicago, Chicago, Illinois 60637, United States; Department of Chemistry and Institute for Biophysical Dynamics, The University of Chicago, Chicago, Illinois 60637, United States; Joint Center for Energy Storage Research, Argonne National Laboratory, Lemont, Illinois 60439, United States; [orcid.org/0000-0003-2895-7915](https://orcid.org/0000-0003-2895-7915)

**Nicholas H. C. Lewis** – James Franck Institute, The University of Chicago, Chicago, Illinois 60637, United States; Department of Chemistry and Institute for Biophysical Dynamics, The University of Chicago, Chicago, Illinois 60637, United States; Joint Center for Energy Storage Research, Argonne National Laboratory, Lemont, Illinois 60439, United States; [orcid.org/0000-0002-2554-0199](https://orcid.org/0000-0002-2554-0199)

**Yong Zhang** – Joint Center for Energy Storage Research, Argonne National Laboratory, Lemont, Illinois 60439, United States; Department of Chemical and Biomolecular Engineering, University of Notre Dame, Notre Dame, Indiana 46556, United States; [orcid.org/0000-0003-3988-5961](https://orcid.org/0000-0003-3988-5961)

**Nathan T. Hahn** – Joint Center for Energy Storage Research, Argonne National Laboratory, Lemont, Illinois 60439, United States; Material, Physical and Chemical Sciences Center, Sandia National Laboratories, Albuquerque, New Mexico 87185, United States; [orcid.org/0000-0001-6187-4068](https://orcid.org/0000-0001-6187-4068)

**Jonathan H. Keim** – Department of Chemistry, The University of Chicago, Chicago, Illinois 60637, United States

**Scott A. Snyder** – Department of Chemistry, The University of Chicago, Chicago, Illinois 60637, United States; [orcid.org/0000-0003-3594-8769](https://orcid.org/0000-0003-3594-8769)

**Edward J. Maginn** – Joint Center for Energy Storage Research, Argonne National Laboratory, Lemont, Illinois 60439, United States; Department of Chemical and Biomolecular Engineering, University of Notre Dame, Notre Dame, Indiana 46556, United States; [orcid.org/0000-0002-6309-1347](https://orcid.org/0000-0002-6309-1347)

Complete contact information is available at: <https://pubs.acs.org/doi/10.1021/jacs.2c00154>

## Notes

The authors declare no competing financial interest.

## ■ ACKNOWLEDGMENTS

This work was supported by the U.S. Department of Energy, Office of Science, Basic Energy Sciences, through the Joint Center for Energy Storage Research (Contract DE-AC0206CH11357) and through grant DE-SC0014305 to A.T. B.D. acknowledges the support from the Swiss National Science Foundation through Postdoc.Mobility fellowship grant P400P2\_180765. Y.Z. and E.J.M. thank the Center for Research Computing (CRC) at the University of Notre Dame for providing computational resources. J.H.K. and S.A.S. thank Dr. Josh Kurutz and Dr. C. Jin Qin for assistance with NMR and mass spectrometry, respectively, and Prof. Jose Ignacio Garcia-Alonso for assistance with the determination of isotopic purity of CD<sub>3</sub><sup>13</sup>CN. Sandia National Laboratories is a multimission laboratory managed and operated by the National Technology and Engineering Solutions of Sandia, LLC, a wholly owned subsidiary of Honeywell International Inc., for the U.S. Department of Energy's National Security Administration under contract DE-NA0003525. This paper describes objective technical results and analysis. Any subjective views or opinions that might be expressed in this paper do not necessarily represent the views of the U.S. Department of Energy or the U.S. Government.

## ■ REFERENCES

- (1) Obama, B. The Irreversible Momentum of Clean Energy. *Science* **2017**, *355*, 126–129.
- (2) Yang, Z.; Zhang, J.; Kintner-Meyer, M. C. W.; Lu, X.; Choi, D.; Lemmon, J. P.; Liu, J. Electrochemical Energy Storage for Green Grid. *Chem. Rev.* **2011**, *111*, 3577–3613.
- (3) Cano, Z. P.; Banham, D.; Ye, S.; Hintennach, A.; Lu, J.; Fowler, M.; Chen, Z. Batteries and Fuel Cells for Emerging Electric Vehicle Markets. *Nat. Energy* **2018**, *3*, 279–289.
- (4) Liang, Y.; Zhao, C.; Yuan, H.; Chen, Y.; Zhang, W.; Huang, J.; Yu, D.; Liu, Y.; Titirici, M.; Chueh, Y.; Yu, H.; Zhang, Q. A Review of Rechargeable Batteries for Portable Electronic Devices. *InfoMat* **2019**, *1*, 6–32.
- (5) Xu, K. Nonaqueous Liquid Electrolytes for Lithium-Based Rechargeable Batteries. *Chem. Rev.* **2004**, *104*, 4303–4418.
- (6) Xu, K. Electrolytes and Interphases in Li-Ion Batteries and Beyond. *Chem. Rev.* **2014**, *114*, 11503–11618.
- (7) Choi, N.-S.; Chen, Z.; Freunberger, S. A.; Ji, X.; Sun, Y.-K.; Amine, K.; Yushin, G.; Nazar, L. F.; Cho, J.; Bruce, P. G. Challenges Facing Lithium Batteries and Electrical Double-Layer Capacitors. *Angew. Chem., Int. Ed.* **2012**, *51*, 9994–10024.
- (8) Li, M.; Wang, C.; Chen, Z.; Xu, K.; Lu, J. New Concepts in Electrolytes. *Chem. Rev.* **2020**, *120*, 6783–6819.
- (9) Choi, J. W.; Aurbach, D. Promise and Reality of Post-Lithium-Ion Batteries with High Energy Densities. *Nat. Rev. Mater.* **2016**, *1*, No. 16013.
- (10) Muldoon, J.; Bucur, C. B.; Gregory, T. Quest for Nonaqueous Multivalent Secondary Batteries: Magnesium and Beyond. *Chem. Rev.* **2014**, *114*, 11683–11720.
- (11) Gummow, R. J.; Vamvounis, G.; Kannan, M. B.; He, Y. Calcium-Ion Batteries: Current State-of-the-Art and Future Perspectives. *Adv. Mater.* **2018**, *30*, No. 1801702.
- (12) Jia, X.; Liu, C.; Neale, Z. G.; Yang, J.; Cao, G. Active Materials for Aqueous Zinc Ion Batteries: Synthesis, Crystal Structure, Morphology, and Electrochemistry. *Chem. Rev.* **2020**, *120*, 7795–7866.
- (13) Zhang, N.; Chen, X.; Yu, M.; Niu, Z.; Cheng, F.; Chen, J. Materials Chemistry for Rechargeable Zinc-Ion Batteries. *Chem. Soc. Rev.* **2020**, *49*, 4203–4219.

- (14) Yamada, Y.; Wang, J.; Ko, S.; Watanabe, E.; Yamada, A. Advances and Issues in Developing Salt-Concentrated Battery Electrolytes. *Nat. Energy* **2019**, *4*, 269–280.
- (15) Borodin, O.; Self, J.; Persson, K. A.; Wang, C.; Xu, K. Uncharted Waters: Super-Concentrated Electrolytes. *Joule* **2020**, *4*, 69–100.
- (16) Doyle, M.; Fuller, T. F.; Newman, J. The Importance of the Lithium Ion Transference Number in Lithium/Polymer Cells. *Electrochim. Acta* **1994**, *39*, 2073–2081.
- (17) Suo, L.; Borodin, O.; Gao, T.; Olguin, M.; Ho, J.; Fan, X.; Luo, C.; Wang, C.; Xu, K. “Water-in-Salt” Electrolyte Enables High-Voltage Aqueous Lithium-Ion Chemistries. *Science* **2015**, *350*, 938–943.
- (18) Yamada, Y.; Furukawa, K.; Sodeyama, K.; Kikuchi, K.; Yaegashi, M.; Tateyama, Y.; Yamada, A. Unusual Stability of Acetonitrile-Based Superconcentrated Electrolytes for Fast-Charging Lithium-Ion Batteries. *J. Am. Chem. Soc.* **2014**, *136*, 5039–5046.
- (19) McOwen, D. W.; Seo, D. M.; Borodin, O.; Vatamanu, J.; Boyle, P. D.; Henderson, W. A. Concentrated Electrolytes: Decrypting Electrolyte Properties and Reassessing Al Corrosion Mechanisms. *Energy Environ. Sci.* **2014**, *7*, 416–426.
- (20) Suo, L.; Borodin, O.; Gao, T.; Olguin, M.; Ho, J.; Fan, X.; Luo, C.; Wang, C.; Xu, K. “Water-in-Salt” Electrolyte Enables High-Voltage Aqueous Lithium-Ion Chemistries. *Science* **2015**, *350*, 938–943.
- (21) Borodin, O.; Suo, L.; Gobet, M.; Ren, X.; Wang, F.; Faraone, A.; Peng, J.; Olguin, M.; Schroeder, M.; Ding, M. S.; Gobrogge, E.; von Wald Cresce, A.; Munoz, S.; Dura, J. A.; Greenbaum, S.; Wang, C.; Xu, K. Liquid Structure with Nano-Heterogeneity Promotes Cationic Transport in Concentrated Electrolytes. *ACS Nano* **2017**, *11*, 10462–10471.
- (22) Dokko, K.; Watanabe, D.; Ugata, Y.; Thomas, M. L.; Tsuzuki, S.; Shinoda, W.; Hashimoto, K.; Ueno, K.; Umebayashi, Y.; Watanabe, M. Direct Evidence for Li Ion Hopping Conduction in Highly Concentrated Sulfolane-Based Liquid Electrolytes. *J. Phys. Chem. B* **2018**, *122*, 10736–10745.
- (23) Zhang, Y.; Lewis, N. H. C.; Mars, J.; Wan, G.; Weadock, N. J.; Takacs, C. J.; Lukatskaya, M. R.; Steinrück, H.-G.; Toney, M. F.; Tokmakoff, A.; Maginn, E. J. Water-in-Salt LiTFSI Aqueous Electrolytes. I. Liquid Structure from Combined Molecular Dynamics Simulation and Experimental Studies. *J. Phys. Chem. B* **2021**, *125*, 4501–4513.
- (24) Ekelin, K.; Sillén, L. G.; Bánhidí, Z. G.; Virtanen, A. I.; Sörensen, N. A. Studies on Ionic Solutions in Diethyl Ether. IV. Properties of LiClO<sub>4</sub>-Ether Solutions. *Acta Chem. Scand.* **1953**, *7*, 987–1000.
- (25) Yuan, S.; Bao, J. L.; Wei, J.; Xia, Y.; Truhlar, D. G.; Wang, Y. A Versatile Single-Ion Electrolyte with a Grotthuss-like Li Conduction Mechanism for Dendrite-Free Li Metal Batteries. *Energy Environ. Sci.* **2019**, *12*, 2741–2750.
- (26) Zhao, Q.; Stalin, S.; Zhao, C.-Z.; Archer, L. A. Designing Solid-State Electrolytes for Safe, Energy-Dense Batteries. *Nat. Rev. Mater.* **2020**, *5*, 229–252.
- (27) Zhang, H.; Li, C.; Piszcz, M.; Coya, E.; Rojo, T.; Rodriguez-Martinez, L. M.; Armand, M.; Zhou, Z. Single Lithium-Ion Conducting Solid Polymer Electrolytes: Advances and Perspectives. *Chem. Soc. Rev.* **2017**, *46*, 797–815.
- (28) Tang, Z.-K.; Tse, J. S.; Liu, L.-M. Unusual Li-Ion Transfer Mechanism in Liquid Electrolytes: A First-Principles Study. *J. Phys. Chem. Lett.* **2016**, *7*, 4795–4801.
- (29) Okoshi, M.; Chou, C.-P.; Nakai, H. Theoretical Analysis of Carrier Ion Diffusion in Superconcentrated Electrolyte Solutions for Sodium-Ion Batteries. *J. Phys. Chem. B* **2018**, *122*, 2600–2609.
- (30) Yim, C.-H.; Tam, J.; Soboleski, H.; Abu-Lebdeh, Y. On the Correlation between Free Volume, Phase Diagram and Ionic Conductivity of Aqueous and Non-Aqueous Lithium Battery Electrolyte Solutions over a Wide Concentration Range. *J. Electrochem. Soc.* **2017**, *164*, A1002–A1011.
- (31) Seo, D. M.; Borodin, O.; Balogh, D.; O’Connell, M.; Ly, Q.; Han, S.-D.; Passerini, S.; Henderson, W. A. Electrolyte Solvation and Ionic Association III. Acetonitrile-Lithium Salt Mixtures—Transport Properties. *J. Electrochem. Soc.* **2013**, *160*, A1061–A1070.
- (32) Forsyth, M.; Yoon, H.; Chen, F.; Zhu, H.; MacFarlane, D. R.; Armand, M.; Howlett, P. C. Novel Na<sup>+</sup> Ion Diffusion Mechanism in Mixed Organic–Inorganic Ionic Liquid Electrolyte Leading to High Na<sup>+</sup> Transference Number and Stable, High Rate Electrochemical Cycling of Sodium Cells. *J. Phys. Chem. C* **2016**, *120*, 4276–4286.
- (33) Alvarado, J.; Schroeder, M. A.; Zhang, M.; Borodin, O.; Gobrogge, E.; Olguin, M.; Ding, M. S.; Gobet, M.; Greenbaum, S.; Meng, Y. S.; Xu, K. A Carbonate-Free, Sulfone-Based Electrolyte for High-Voltage Li-Ion Batteries. *Mater. Today* **2018**, *21*, 341–353.
- (34) Kondou, S.; Thomas, M. L.; Mandai, T.; Ueno, K.; Dokko, K.; Watanabe, M. Ionic Transport in Highly Concentrated Lithium Bis(Fluorosulfonyl)Amide Electrolytes with Keto Ester Solvents: Structural Implications for Ion Hopping Conduction in Liquid Electrolytes. *Phys. Chem. Chem. Phys.* **2019**, *21*, 5097–5105.
- (35) Ugata, Y.; Thomas, M. L.; Mandai, T.; Ueno, K.; Dokko, K.; Watanabe, M. Li-Ion Hopping Conduction in Highly Concentrated Lithium Bis(Fluorosulfonyl)Amide/Dinitrile Liquid Electrolytes. *Phys. Chem. Chem. Phys.* **2019**, *21*, 9759–9768.
- (36) Ugata, Y.; Sasagawa, S.; Tataru, R.; Ueno, K.; Watanabe, M.; Dokko, K. Structural Effects of Solvents on Li-Ion-Hopping Conduction in Highly Concentrated LiBF<sub>4</sub>/Sulfone Solutions. *J. Phys. Chem. B* **2021**, *125*, 6600–6608.
- (37) Moilanen, D. E.; Wong, D.; Rosenfeld, D. E.; Fenn, E. E.; Fayer, M. D. Ion-Water Hydrogen-Bond Switching Observed with 2D IR Vibrational Echo Chemical Exchange Spectroscopy. *Proc. Natl. Acad. Sci. U.S.A.* **2009**, *106*, 375–380.
- (38) Fayer, M. D.; Moilanen, D. E.; Wong, D.; Rosenfeld, D. E.; Fenn, E. E.; Park, S. Water Dynamics in Salt Solutions Studied with Ultrafast Two-Dimensional Infrared (2D IR) Vibrational Echo Spectroscopy. *Acc. Chem. Res.* **2009**, *42*, 1210–1219.
- (39) Kwon, Y.; Park, S. Complexation Dynamics of CH<sub>3</sub>SCN and Li<sup>+</sup> in Acetonitrile Studied by Two-Dimensional Infrared Spectroscopy. *Phys. Chem. Chem. Phys.* **2015**, *17*, 24193–24200.
- (40) Yuan, R.; Yan, C.; Fayer, M. Ion–Molecule Complex Dissociation and Formation Dynamics in LiCl Aqueous Solutions from 2D IR Spectroscopy. *J. Phys. Chem. B* **2018**, *122*, 10582–10592.
- (41) Yuan, R.; Fayer, M. D. Dynamics of Water Molecules and Ions in Concentrated Lithium Chloride Solutions Probed with Ultrafast 2D IR Spectroscopy. *J. Phys. Chem. B* **2019**, *123*, 7628–7639.
- (42) Lee, K.-K.; Park, K.; Lee, H.; Noh, Y.; Kossowska, D.; Kwak, K.; Cho, M. Ultrafast Fluxional Exchange Dynamics in Electrolyte Solvation Sheath of Lithium Ion Battery. *Nat. Commun.* **2017**, *8*, No. 14658.
- (43) Zhang, M.; Hao, H.; Zhou, D.; Duan, Y.; Wang, Y.; Bian, H. Understanding the Microscopic Structure of a “Water-in-Salt” Lithium Ion Battery Electrolyte Probed with Ultrafast IR Spectroscopy. *J. Phys. Chem. C* **2020**, *124*, 8594–8604.
- (44) Lewis, N. H. C.; Zhang, Y.; Dereka, B.; Carino, E.; Maginn, E. J.; Tokmakoff, A. Signatures of Ion Pairing and Aggregation in the Vibrational Spectroscopy of Super-Concentrated Aqueous Lithium Bistriflimide Solutions. *J. Phys. Chem. C* **2020**, *124*, 3470–3481.
- (45) Biswas, A.; Mallik, B. S. Ultrafast Aqueous Dynamics in Concentrated Electrolytic Solutions of Lithium Salt and Ionic Liquid. *J. Phys. Chem. B* **2020**, *124*, 9898–9912.
- (46) Chen, X.; Kuroda, D. G. Molecular Motions of Acetonitrile Molecules in the Solvation Shell of Lithium Ions. *J. Chem. Phys.* **2020**, *153*, No. 164502.
- (47) Zhang, X.; Kuroda, D. G. An Ab Initio Molecular Dynamics Study of the Solvation Structure and Ultrafast Dynamics of Lithium Salts in Organic Carbonates: A Comparison between Linear and Cyclic Carbonates. *J. Chem. Phys.* **2019**, *150*, No. 184501.
- (48) Fulfer, K. D.; Kuroda, D. G. Ion Speciation of Lithium Hexafluorophosphate in Dimethyl Carbonate Solutions: An Infrared Spectroscopy Study. *Phys. Chem. Chem. Phys.* **2018**, *20*, 22710–22718.
- (49) Liang, C.; Kwak, K.; Cho, M. Revealing the Solvation Structure and Dynamics of Carbonate Electrolytes in Lithium-Ion Batteries by

- Two-Dimensional Infrared Spectrum Modeling. *J. Phys. Chem. Lett.* **2017**, *8*, 5779–5784.
- (50) Lim, J.; Lee, K.-K.; Liang, C.; Park, K.-H.; Kim, M.; Kwak, K.; Cho, M. Two-Dimensional Infrared Spectroscopy and Molecular Dynamics Simulation Studies of Nonaqueous Lithium Ion Battery Electrolytes. *J. Phys. Chem. B* **2019**, *123*, 6651–6663.
- (51) Galle Kankanamge, S. R.; Kuroda, D. G. Molecular Structure, Chemical Exchange, and Conductivity Mechanism of High Concentration LiTFSI Electrolytes. *J. Phys. Chem. B* **2020**, *124*, 1965–1977.
- (52) Chen, X.; Fulfer, K. D.; Woodard, K. T.; Kuroda, D. G. Structure and Dynamics of the Lithium-Ion Solvation Shell in Ureas. *J. Phys. Chem. B* **2019**, *123*, 9889–9898.
- (53) Rushing, J. C.; Leonik, F. M.; Kuroda, D. G. Effect of Solvation Shell Structure and Composition on Ion Pair Formation: The Case Study of LiTDI in Organic Carbonates. *J. Phys. Chem. C* **2019**, *123*, 25102–25112.
- (54) Fulfer, K. D.; Kuroda, D. G. Solvation Structure and Dynamics of the Lithium Ion in Organic Carbonate-Based Electrolytes: A Time-Dependent Infrared Spectroscopy Study. *J. Phys. Chem. C* **2016**, *120*, 24011–24022.
- (55) Fulfer, K. D.; Galle Kankanamge, S. R.; Chen, X.; Woodard, K. T.; Kuroda, D. G. Elucidating the Mechanism behind the Infrared Spectral Features and Dynamics Observed in the Carbonyl Stretch Region of Organic Carbonates Interacting with Lithium Ions. *J. Chem. Phys.* **2021**, *154*, No. 234504.
- (56) Chen, H.; Wen, X.; Guo, X.; Zheng, J. Intermolecular Vibrational Energy Transfers in Liquids and Solids. *Phys. Chem. Chem. Phys.* **2014**, *16*, 13995–14014.
- (57) Reichardt, C.; Welton, T. *Solvents and Solvent Effects in Organic Chemistry*, 4th ed.; Wiley-VCH Verlag & Co., 2011.
- (58) Riddlestone, I. M.; Kraft, A.; Schaefer, J.; Krossing, I. Taming the Cationic Beast: Novel Developments in the Synthesis and Application of Weakly Coordinating Anions. *Angew. Chem., Int. Ed.* **2018**, *57*, 13982–14024.
- (59) Wang, F.; Borodin, O.; Gao, T.; Fan, X.; Sun, W.; Han, F.; Faraoane, A.; Dura, J. A.; Xu, K.; Wang, C. Highly Reversible Zinc Metal Anode for Aqueous Batteries. *Nat. Mater.* **2018**, *17*, 543–549.
- (60) Zeng, P.; Han, Y.; Duan, X.; Jia, G.; Huang, L.; Chen, Y. A Stable Graphite Electrode in Superconcentrated LiTFSI-DME/DOL Electrolyte and Its Application in Lithium-Sulfur Full Battery. *Mater. Res. Bull.* **2017**, *95*, 61–70.
- (61) Chen, L.; Zhang, J.; Li, Q.; Vatamanu, J.; Ji, X.; Pollard, T. P.; Cui, C.; Hou, S.; Chen, J.; Yang, C.; Ma, L.; Ding, M. S.; Garaga, M.; Greenbaum, S.; Lee, H.-S.; Borodin, O.; Xu, K.; Wang, C. A 63 m Superconcentrated Aqueous Electrolyte for High-Energy Li-Ion Batteries. *ACS Energy Lett.* **2020**, *5*, 968–974.
- (62) Yamada, Y.; Chiang, C. H.; Sodeyama, K.; Wang, J.; Tateyama, Y.; Yamada, A. Corrosion Prevention Mechanism of Aluminum Metal in Superconcentrated Electrolytes. *ChemElectroChem* **2015**, *2*, 1687–1694.
- (63) Kwon, Y.; Lee, C.; Park, S. Effect of Ion–Molecule Interaction on Fermi-Resonance in Acetonitrile Studied by Ultrafast Vibrational Spectroscopy. *Chem. Phys.* **2014**, *445*, 38–45.
- (64) Yuan, K.; Bian, H.; Shen, Y.; Jiang, B.; Li, J.; Zhang, Y.; Chen, H.; Zheng, J. Coordination Number of Li<sup>+</sup> in Nonaqueous Electrolyte Solutions Determined by Molecular Rotational Measurements. *J. Phys. Chem. B* **2014**, *118*, 3689–3695.
- (65) Dereka, B.; Lewis, N. H. C.; Keim, J. H.; Snyder, S. A.; Tokmakoff, A. Characterization of Acetonitrile Isotopologues as Vibrational Probes of Electrolytes. *J. Phys. Chem. B* **2022**, *126*, 278–291.
- (66) Deak, J. C.; Iwaki, L. K.; Dlott, D. D. Vibrational Energy Redistribution in Polyatomic Liquids: Ultrafast IR–Raman Spectroscopy of Acetonitrile. *J. Phys. Chem. A* **1998**, *102*, 8193–8201.
- (67) Deak, J. C.; Iwaki, L. K.; Rhea, S. T.; Dlott, D. D. Ultrafast Infrared-Raman Studies of Vibrational Energy Redistribution in Polyatomic Liquids. *J. Raman Spectrosc.* **2000**, *31*, 263–274.
- (68) Fini, G.; Mirono, P. On the Secondary Structure of Some Vibrational Bands of Acetonitrile. *Spectrochim. Acta, Part A* **1976**, *32*, 439–440.
- (69) Besnard, M.; Isabel Cabaço, M.; Strehle, F.; Yarwood, J. Raman Spectroscopic Studies on the Dynamic and Equilibrium Processes in Binary Mixtures Containing Methanol and Acetonitrile. *Chem. Phys.* **1992**, *163*, 103–114.
- (70) Cho, M. *Two-Dimensional Optical Spectroscopy*; CRC Press, 2009.
- (71) De Marco, L.; Fournier, J. A.; Thämer, M.; Carpenter, W.; Tokmakoff, A. Anharmonic Exciton Dynamics and Energy Dissipation in Liquid Water from Two-Dimensional Infrared Spectroscopy. *J. Chem. Phys.* **2016**, *145*, No. 094501.
- (72) Zheng, J.; Kwak, K.; Fayer, M. D. Ultrafast 2D IR Vibrational Echo Spectroscopy. *Acc. Chem. Res.* **2007**, *40*, 75–83.
- (73) Zheng, J.; Kwak, K.; Asbury, J.; Chen, X.; Piletic, I. R.; Fayer, M. D. Ultrafast Dynamics of Solute-Solvent Complexation Observed at Thermal Equilibrium in Real Time. *Science* **2005**, *309*, 1338–1343.
- (74) Kwak, K.; Park, S.; Fayer, M. D. Dynamics around Solutes and Solute Solvent Complexes in Mixed Solvents. *Proc. Natl. Acad. Sci. U.S.A.* **2007**, *104*, 14221–14226.
- (75) Dunbar, J. A.; Arthur, E. J.; White, A. M.; Kubarych, K. J. Ultrafast 2D-IR and Simulation Investigations of Preferential Solvation and Cosolvent Exchange Dynamics. *J. Phys. Chem. B* **2015**, *119*, 6271–6279.
- (76) Kiefer, L. M.; Kubarych, K. J. Solvent Exchange in Preformed Photocatalyst-Donor Precursor Complexes Determines Efficiency. *Chem. Sci.* **2018**, *9*, 1527–1533.
- (77) Rosenfeld, D. E.; Gengeliczi, Z.; Smith, B. J.; Stack, T. D. P.; Fayer, M. D. Structural Dynamics of a Catalytic Monolayer Probed by Ultrafast 2D IR Vibrational Echoes. *Science* **2011**, *334*, 634–639.
- (78) Rosenfeld, D. E.; Fayer, M. D. Excitation Transfer Induced Spectral Diffusion and the Influence of Structural Spectral Diffusion. *J. Chem. Phys.* **2012**, *137*, No. 064109.
- (79) Kameda, Y.; Saito, S.; Saji, A.; Amo, Y.; Usuki, T.; Watanabe, H.; Arai, N.; Umebayashi, Y.; Fujii, K.; Ueno, K.; Ikeda, K.; Otomo, T. Solvation Structure of Li<sup>+</sup> in Concentrated Acetonitrile and *N,N*-Dimethylformamide Solutions Studied by Neutron Diffraction with <sup>6</sup>Li/<sup>7</sup>Li Isotopic Substitution Methods. *J. Phys. Chem. B* **2020**, *124*, 10456–10464.
- (80) Génereux, S.; Gariépy, V.; Rochefort, D. On the Relevance of Reporting Water Content in Highly Concentrated Electrolytes: The LiTFSI-Acetonitrile Case. *J. Electrochem. Soc.* **2020**, *167*, No. 120536.
- (81) Zhang, Y.; Maginn, E. J. Water-In-Salt LiTFSI Aqueous Electrolytes (2): Transport Properties and Li<sup>+</sup> Dynamics Based on Molecular Dynamics Simulations. *J. Phys. Chem. B* **2021**, *125*, 13246–13254.
- (82) Self, J.; Fong, K. D.; Persson, K. A. Transport in Superconcentrated LiPF<sub>6</sub> and LiBF<sub>4</sub> /Propylene Carbonate Electrolytes. *ACS Energy Lett.* **2019**, *4*, 2843–2849.
- (83) Chen, H.; Bian, H.; Li, J.; Wen, X.; Zhang, Q.; Zhuang, W.; Zheng, J. Vibrational Energy Transfer: An Angstrom Molecular Ruler in Studies of Ion Pairing and Clustering in Aqueous Solutions. *J. Phys. Chem. B* **2015**, *119*, 4333–4349.
- (84) Rubtsov, I. V. Relaxation-Assisted Two-Dimensional Infrared (RA 2DIR) Method: Accessing Distances over 10 Å and Measuring Bond Connectivity Patterns. *Acc. Chem. Res.* **2009**, *42*, 1385–1394.
- (85) Kurochkin, D. V.; Naraharisetty, S. R. G.; Rubtsov, I. V. A Relaxation-Assisted 2D IR Spectroscopy Method. *Proc. Natl. Acad. Sci. U.S.A.* **2007**, *104*, 14209–14214.
- (86) Panman, M. R.; Bakker, B. H.; den Uyl, D.; Kay, E. R.; Leigh, D. A.; Buma, W. J.; Brouwer, A. M.; Geenevasen, J. A. J.; Woutersen, S. Water Lubricates Hydrogen-Bonded Molecular Machines. *Nat. Chem.* **2013**, *5*, 929–934.
- (87) Alfurayj, I.; Fraenza, C. C.; Zhang, Y.; Pandian, R.; Spittle, S.; Hansen, B.; Dean, W.; Gurkan, B.; Savinell, R.; Greenbaum, S.; Maginn, E.; Sangoro, J.; Burda, C. Solvation Dynamics of Wet Ethaline: Water Is the Magic Component. *J. Phys. Chem. B* **2021**, *125*, 8888–8901.

(88) Horng, M. L.; Gardecki, J.; Papazyan, A.; Maroncelli, M. Subpicosecond Measurements of Polar Solvation Dynamics: Coumarin 153 Revisited. *J. Phys. Chem. A* **1995**, *99*, 17311–17337.

(89) Loughnane, B. J.; Scodinu, A.; Farrer, R. A.; Fourkas, J. T.; Mohanty, U. Exponential Intermolecular Dynamics in Optical Kerr Effect Spectroscopy of Small-Molecule Liquids. *J. Chem. Phys.* **1999**, *111*, 2686–2694.

(90) Sawayama, S.; Ochi, R.; Mimura, H.; Morita, M.; Fujii, K. 2,2,2-Trifluoroethyl Acetate as an Electrolyte Solvent for Lithium-Ion Batteries: Effect of Weak Solvation on Electrochemical and Structural Characteristics. *J. Phys. Chem. C* **2021**, *125*, 27098–27105.

(91) Dokko, K.; Tachikawa, N.; Yamauchi, K.; Tsuchiya, M.; Yamazaki, A.; Takashima, E.; Park, J.-W.; Ueno, K.; Seki, S.; Serizawa, N.; Watanabe, M. Solvate Ionic Liquid Electrolyte for Li–S Batteries. *J. Electrochem. Soc.* **2013**, *160*, A1304–A1310.

(92) Holoubek, J.; Liu, H.; Wu, Z.; Yin, Y.; Xing, X.; Cai, G.; Yu, S.; Zhou, H.; Pascal, T. A.; Chen, Z.; Liu, P. Tailoring Electrolyte Solvation for Li Metal Batteries Cycled at Ultra-Low Temperature. *Nat. Energy* **2021**, *6*, 303–313.

(93) Baskin, A.; Lawson, J. W.; Prendergast, D. Anion-Assisted Delivery of Multivalent Cations to Inert Electrodes. *J. Phys. Chem. Lett.* **2021**, *12*, 4347–4356.